CrystEngComm

ROYAL SOCIETY OF CHEMISTRY

COMMUNICATION

View Article Online
View Journal | View Issue

Check for updates

Cite this: *CrystEngComm*, 2025, **27**, 4463

Received 17th March 2025,
Accepted 9th June 2025

DOI: 10.1039/d5ce00299k

rsc.li/crystengcomm

A multivariate library of zirconia metal–organic frameworks with dissolved *p*-nitroaniline dipoles and concentration-dependent optical and dielectric response†

Kyle R. Langlois,[ab] Yangyang Wang,[c] Fnu Joshua,[ad] Wesley J. Newsome,[a] Lei Zhai,[ad] James K. Harper[e] and Fernando J. Uribe-Romo *[ab]

In this work, we show how the combination of soluble non-polar and polar links allows for the preparation of multivariate metal–organic frameworks (MTV MOFs) that exhibit dipolar solid-solution behavior. We prepared a library of PIZOF-2 MOFs with varied concentrations of *p*-nitroaniline (PNA)-containing moiety embedded within the MTV links. This library forms a partial solid solution up to 30 mol% with input/output composition ratio of 0.536 ± 0.018. MOFs with $x > 5$ mol% PNA show concentration-dependent hypsochromic dipole–dipole coupling (H-coupling) in the solid-state UV-visible spectra. The MTV library also exhibits a dielectric relaxation event in the broadband dielectric spectra with activation enthalpies and entropies that vary with temperature and PNA content and follow linear Meyer–Neldel compensation relations.

Introduction

Multivariate metal–organic frameworks (MTV MOFs) are isoreticular crystals formed from mixtures of organic links.[1,2] The ability to vary the composition of a MOF while keeping a constant crystal structure has made them perfect candidates for systematic studies as matrices in MOF-based substitutional solid-solutions. This is achieved by using soluble organic links that form MOFs with simple topological structures. We have shown that the family of porous interpenetrated zirconia organic frameworks, PIZOFs, are excellent matrices for solid-solution studies, because they have a simple, default topological structure, high symmetry cubic space group, have exceptional chemical stability, long shelf-life, and high porosity.[3–5] We have demonstrated that solid-solutions of MTV PIZOFs can exhibit solid-state properties that depend on the nature and concentration of predesigned solute links, such as multicolour fluorescence, white-light emission, fluorescence energy transfer,[6–8] redox hopping conductivity,[9] aggregate-induced emission,[10,11] water adsorption,[12] and follow Vegard's law.[13]

In this work, we show the incorporation of molecular π-dipoles as multivariate solute links in a PIZOF matrix, producing a library of crystals that show concentration dependent effects (Fig. 1a). The π-dipoles correspond to *p*-nitroaniline (PNA) incorporated within the central ring of the matrix link (Fig. 1b). PNA is the archetypal example of a dipolar molecule, featuring a donor–π–acceptor (or push/pull) electronic structure that produces strong polarity,[14,15] and it has been extensively studied in liquid solutions, polymer blends, and porous solids.[16–24] We hypothesized that systematic incorporation of PNA building blocks as solute components in MTV MOF matrices resulted in MOFs that have variable bulk polarity. The multivariate crystals were characterized using solid-state optical and dielectric spectroscopies, observing concentration-dependent dipole–dipole hypsochromic coupling and dielectric relaxation with thermodynamic parameters of activated state that depend on PNA content. We demonstrate how targeting molecular traits in solute links enable the study of their solution-like behaviour in the solid state.

Results and discussion

The polar link was synthesized by consecutive protection/nitration/deprotection of 2,5-dibromoaniline, followed by Sonogashira coupling with 4-ethynyl benzoate ester and hydrolysis in base, producing **H_2PEPEP-PNA**, (section S2†). The matrix link was prepared following published procedures.[7] The multivariate library was prepared by mixing links at varied molar ratios in solvothermal glass reactors with $ZrCl_4$, proline,

[a] *Department of Chemistry, University of Central Florida, Orlando, FL 32814, USA. E-mail: fernando@ucf.edu*
[b] *REACT: Renewable Energy and Chemical Transformations Cluster, University of Central Florida, Orlando, FL 32814, USA*
[c] *Center for Nanophase Materials Sciences, Oak Ridge National Laboratory, Oak Ridge, TN 37831, USA*
[d] *NanoScience Technology Center, University of Central Florida, Orlando, FL 32814, USA*
[e] *Department of Chemistry, University of Utah, Salt Lake City, UT 84112, USA*

† Electronic supplementary information (ESI) available: Synthesis, powder crystallography, materials characterization, optical and dielectric spectra, CCDC 2455083. See DOI: https://doi.org/10.1039/d5ce00299k

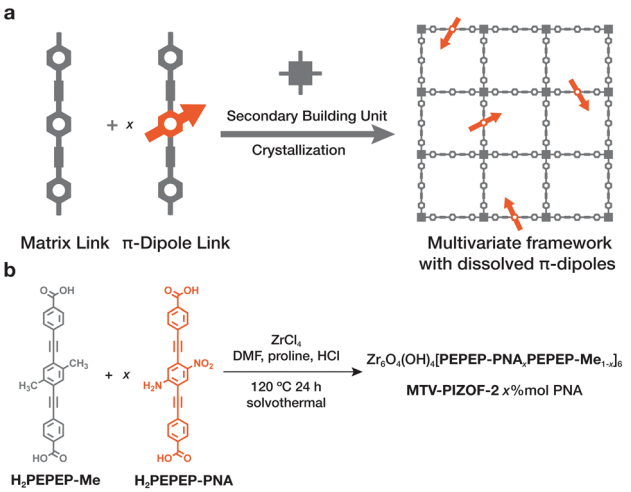

Fig. 1 (a) MTV MOF library with varied concentration of dipolar links in the MOF matrix. (b) Synthesis of a dipolar MTV MOF library with *p*-nitroaniline as solute dipole.

and HCl in DMF at 120 °C for 2 d affording the MTV MOF library, with formulas $Zr_6O_4(OH)_4$[**PEPEP-PNA**$_x$**PEPEP**-Me$_{1-x}$]$_6$ (section S2†). We observed crystal formation continuously up to x = 50 mol% input **PEPEP-PNA**, as evidenced by the presence of sharp diffraction lines in the PXRD (Fig. 2a), which match the observed PIZOF-2 MOF ($Fd\bar{3}m$). Under slightly different synthesis conditions, we crystalized the phase with 100 mol% **PEPEP-PNA**. It is important to note the absence of the 200 reflections, this absence is characteristic of the interpenetrated nature of the MOF (section S3†).[3] Samples observed under scanning electron microscopy (SEM) showed octahedral crystals with particle sizes ranging between 1 to 80 μm across all compositions, also exhibiting an overall small particle size distribution (7.4 to 18.8 μm, see section S6†).

Output compositions were determined *via* solution ^{1}H NMR spectroscopy from samples digested in D_2SO_4/DMSO-d_6. Integration of the respective peaks for each link provided input/output (I/O) molar ratios shown in Fig. 2b. In an ideal solid-solution the I/O molar ratios should be one, with deviations due to lower miscibility of the solute links in the matrix. We observed a I/O slope of m = 0.536 ± 0.018 with good linear correlation (R^2 = 0.9906), for ten compositions, in triplicate, up to 50 mol% input, evidencing the formation of a partial solid-solution up to *ca.* 30 mol% output. Having a slope less than one indicates that **PEPEP-PNA** links may not be as miscible in the **PEPEP-Me** matrix, compared to other MTV libraries.[13] Size effects of this matrix-solute immiscibility were noticed when attempting to crystallize a multivariate library using quaterphenyl-dicarboxylate (QPDC) matrix link (PIZOF-1 MOF). In a previous communication,[13] we showed that links of different size may form solid-solutions that follow Vegard's law. However, in the case of QPDC and **PEPEP-PNA**, we observed phase separation, inconsistent solute loadings, and crystal indexing, indicating lower tolerance of **PEPEP-PNA** in the QPDC MOF matrix.

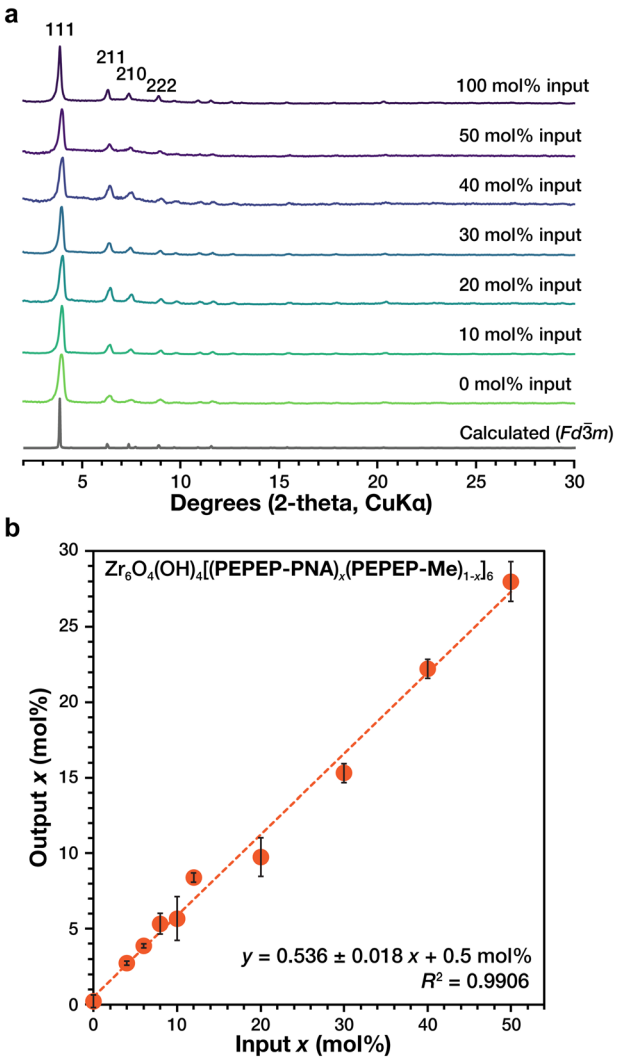

Fig. 2 (a) Powder X-ray diffractograms of PNA MTV MOFs at variable inputs composition. (b) Input/output (I/O) composition relation plot. Note linear trend with slope m = 0.536 ± 0.018. Error bars correspond to the standard deviation of triplicates.

The molecular structure of the MTV library was assessed using vibrational and solid-state NMR spectroscopies (see ESI section S7†). Solid-state ^{13}C CP MAS NMR spectra (Fig. S43†) displays the presence of the expected chemical signals for carboxylates (*ca.* 155 ppm), aromatic (150–110 ppm), alkynes (70 ppm), methyl (5 ppm), and some residual THF guest (55, 20 ppm). Similarly, Raman spectra of the multivariates (Fig. S45†) show the presence of symmetric alkyne stretch at *ca.* 2200 cm^{-1} and carboxylate at *ca.* 1600 cm^{-1}. All the prepared MOFs are porous, exhibiting Brunauer–Emmett–Teller (BET) surface areas in the range S_{BET} = 820–1450 m^2 g^{-1}. The pore size distribution plots obtained from non-local density functional theory (NLDFT) methods exhibited a change in average pore diameter from 22.5 Å in the 0 mol% MOF matrix to 18 Å in the 100 mol% **PEPEP-PNA** MOF. This shift can relate to pore crowding by amino and nitro groups. The mixed-link multivariates display both pore sizes, with a small

contribution by 18 Å pores and large contribution of 22.5 Å pores, consistent with the trend of PNA content. All the prepared MOFs are thermally stable (under N_2) up to around 300–400 °C as determined by thermal gravimetry.

The photo physical properties were probed using solid-state diffuse reflectance UV-visible (DR-UV-vis) spectroscopy. DR-UV-vis measures changes in light reflected by powder samples due to absorption and scattering. A common challenge in the study of powder solids, is to decouple absorption from scattering because it enables the use of solution based theories. Given that we observe similar crystallite size distribution in the SEM (see above), we expect to see minimal or average effect of scattering. According to the theory of light absorption by chromophores in solution, varying the concentration of a solute induces continuous changes in reflectance due to continuous changes in absorption. The changes in absorption are evidenced in the Kubelka–Munk function $F(R(\lambda))$ of the MOFs (1):

$$F(R(\lambda)) = \frac{(1-R(\lambda))^2}{2R(\lambda)} \quad (1)$$

where $R(\lambda)$ is the percent reflectance of a sample as function of wavelength. The $F(R)$ function of the MTV library is shown in Fig. 3 (left), compared to the absorbance spectrum of **PEPEP-PNA** and **PEPEP-Me** diester links in 1,2-dichloroethane. The Kubelka–Munk function of the 0 mol% matrix MOF (Fig. 3, left, yellow trace) exhibits a broad absorption band below 400 nm and low absorption at longer wavelengths. This 400 nm absorption band corresponds to the n → d, or π → d transitions in the zirconia cluster, and remains constant throughout the MTV library with increased **PEPEP-PNA**. Tauc analysis[25] with direct bandgap model determined an optical gap of E_g = 3.00 ± 0.08 eV over ten compositions, including the matrix and the 100 mol% PNA MOF.

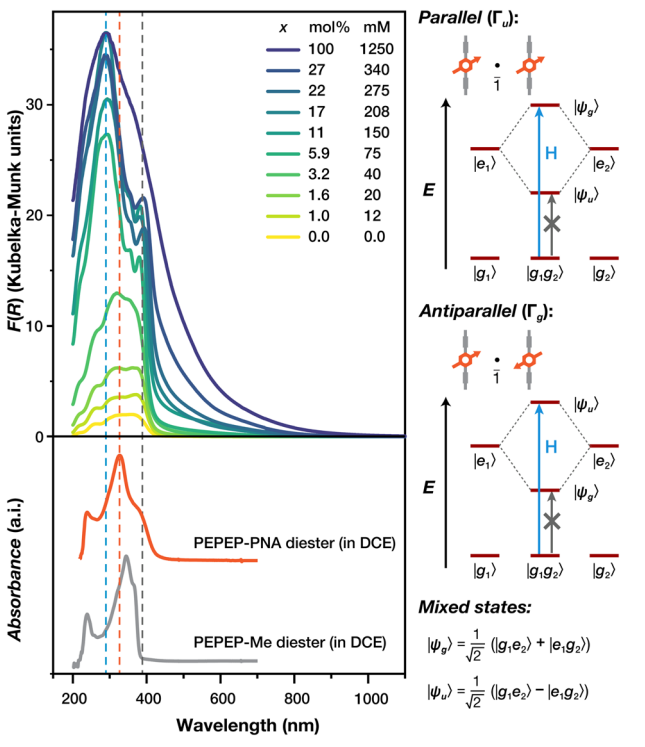

Fig. 3 Kubelka–Munk function from diffuse reflectance UV-visible spectroscopy of the multivariate library, compared to solution-based spectra of the PNA (orange) and matrix (gray) links. Broken lines indicate the bandgap, E_g (right), π–π* transition of PNA (center), and the emergent H-band (left).

The solution-state spectrum of the PNA diester link in 1,2-dichloroethane displays at least three absorption bands below 400 nm with λ_{max} = 350 nm, related to π → π* transitions in the dialkyne-PNA electronic structure.[26] The λ_{max} signal appears in MTV samples with **PEPEP-PNA** concentration up to 3.2 mol% (40 mM based on the average unit cell). At higher **PEPEP-PNA** concentrations, an intense signal at 298 nm appears, displaying significant broadening with increased PNA content and extending up to 700 nm in the 100 mol% sample (1250 mM based on links per unit cell, see section S4†), consistent with broadening due to increased chromophore concentration. Due to the centrosymmetric nature of the MOF matrix (space group $Fd\bar{3}m$), it is possible for two dipoles to interact through space and inversion symmetry *via* hypsochromic dipole–dipole coupling (H-coupling).[27–30] In the crystal structure of PIZOF-2, the central ring of the links occupy the 48f Wyckoff position with local symmetry mm2 (C_{2v}). Since the PNA moiety in the PEPEP link has only m symmetry (C_s), positional disorder in the average unit cell induces equal distribution of $-NH_2$ and $-NO_2$ groups in four available positions. This results in two possible geometric configurations of the ground state, each able to produce coupling. With respect to inversion symmetry, two dipoles can interact in a parallel configuration (Fig. 3, right), with Γ_u representation, and antiparallel with Γ_g representation.[31]

In hypsochromic dipole–dipole coupling, a pair of chromophores in either Γ_g or Γ_u ground states, interact by producing mixed excited states that arise from the tensor product space of two chromophores, each contributing with a ground and a first excited state as basis vectors. In either geometry, the tensor product space results in two possible mixed states, $|\Psi_g\rangle$ and $|\Psi_u\rangle$ (Fig. 3, right), of which only the high energy mixed state ($|\Psi_g\rangle$ in parallel, $|\Psi_u\rangle$ in antiparallel) is allowed by symmetry to be accessed from the ground state. This allowed high energy transition results in an intense signal in the $F(R)$ spectrum of the MTV MOFs with $x > 5$ mol%, with λ_{max} = 298 nm and significant broadening at increased PNA concentration. This signal is shifted by about 32 nm from the main **PEPEP-PNA** transition a 330 nm. Tauc analysis of the H-band in MOFs with $x > 5$ mol% produced an optical energy gap of E_H = 3.40 ± 0.07 eV over six compositions. From the concentration of **PEPEP-PNA** in molar units, (mol_{link} $dm_{MOFcrystal}^{-3}$), the average distance between dipoles correspond to a minimum average distance for detection of H-coupling to be between 28–35 Å (Table S4†). Further evidence of H-coupling was obtained from fluorescence spectroscopy. All MTV samples displayed low

solid-state fluorescence (Fig. S26†), and a similar profile with λ_{max} = 539 ± 2 nm. The 0 mol% matrix emmits with a λ_{max} = 519 nm, and the 100 mol% PNA MOF at λ_{max} = 560 nm. H-coupling is characterized by displaying low fluorescence and no fluorescence shift *vs.* concentration. These observations suggest the MTV library emits from the low-energy mixed state, with no fluorescence shift; in contrast to J-coupling, which shifts the λ_{max} continuously with respect to composition.[31] Future studies include transient absorption and lifetime measurements on larger single crystalline samples to further study the proposed electronic structure.

The dielectric properties of the PNA MTV library were measured in the frequency range of 10^0–10^6 Hz and temperature range of 163 and 293 K using a Novocontrol broadband dielectric spectrometer. The temperature was controlled by a QUATRO cryogenic system (ESI† section S10). The activated MOF samples were loaded in a custom-made plate–plate capacitor cell. In this work, we focus on analyzing the frequency-dependent complex dielectric permittivity (2):

$$\tilde{\varepsilon}(f) = \varepsilon'(f) - i\varepsilon''(f) \quad (2)$$

where the real part $\varepsilon'(f)$ correspond to the dielectric storage (real permittivity), and the imaginary part $\varepsilon''(f)$ to the dielectric losses (absorption), f is the AC frequency and i is the imaginary unit.[32] Capacitive behavior with low losses was observed in all the MTV library, as evidenced by complex phase angles near −90° and small dissipation factors, at all frequencies, and all temperatures. Weak capacitive behavior with low losses is expected in highly porous dielectric crystals. The complex plane representation of dielectric function (Cole–Cole plot) is shown in Fig. 4a and b for 0 and 22 mol% **PEPEP-PNA**. In all samples, capacitive behavior was observed at low temperatures showing resistance at high temperature and low frequencies, evidenced by the combined semicircular and linear shapes in the Cole–Cole plot. This resistance can be assigned to polarization of the electrodes, as observed in similar MOFs.[33]

The frequency-dependent dielectric loss $\varepsilon''(f)$ of all samples (Fig. 4c and S86–S92†), show the appearance of a broad and weak dielectric relaxation signal that peaks at 10^0 Hz at around 190 K and drifts to *ca.* 10^2 Hz at 200 K. Above this temperature, the signal drifts towards 10^6 Hz at 293 K, displaying a noticeable change in drift rate with respect to the lower temperatures (see white arrows in Fig. 4c). This dielectric behavior is similar to that observed in other simple MOFs,[34–37] where the dielectric response is associated with torque around the *p*-phenylene rings of the links as result of quadrupole-electric field gradient interaction. Fitting the functions with the Havriliak–Negami relation for dielectric relaxation provided the characteristic relaxation time (τ). Due to the bulk powder nature of the prepared MTV MOF library, accurate determination of the induced polarization (ε_∞) and dielectric strength ($\Delta\varepsilon$) of the dipoles was not possible.

The dielectric relaxation process follows a thermally activated mechanism as evidenced by the appearance of

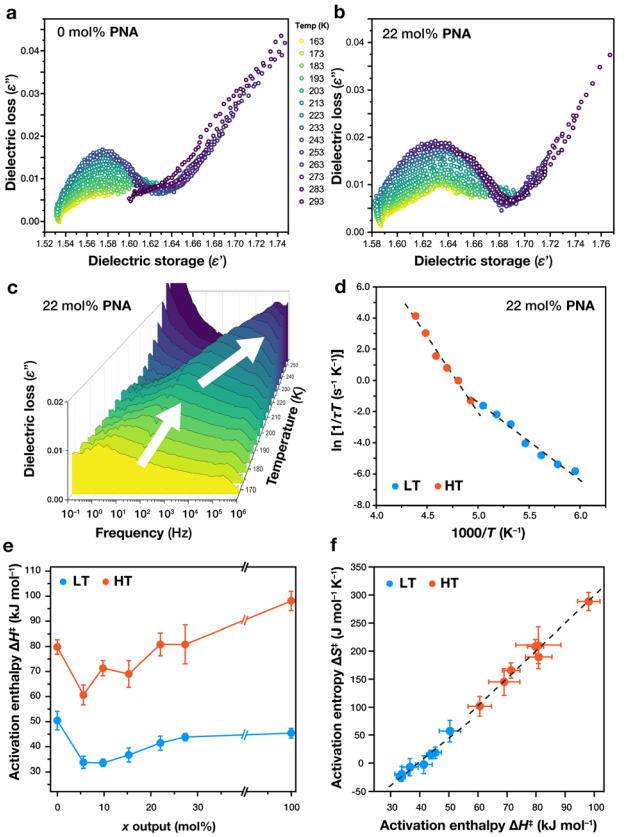

Fig. 4 Cole–Cole plots of (a) 0 mol% PNA and (b) 22 mol% PNA. (c) Bode plot of 22 mol% PNA *vs.* temperature. White arrows accentuate changes in peak drift with temperature. (d) Eyring plot of 22 mol% PNA MOF (e) activation enthalpy from Eyring analysis *vs.* composition for all samples. (f) Meyer–Nelder compensation plot.

linear functions in the Eyring plot of relaxation time *vs.* temperature. Fig. 4d shows the Eyring plot for 22 mol% PNA MOF, exhibiting a linear trend that changes slope at around 200 K, consistent with the observation of signal drift. A change in slope of this kind suggest: a) the appearance of a collective mode of activation at high temperatures, or b) the presence of two relaxation processes that appear at different temperatures. Extraction of the slopes and intercepts for each linear section (LT below 200 K, HT above 200 K) allowed the determination of activation enthalpies, $\Delta H^{\ddagger}$, and entropies, $\Delta S^{\ddagger}$, for each composition (Fig. S95†). The effects of PNA concentration on the dielectric properties of the MTV library can be observed in Fig. 4e (Table S8†). In LT region, the activation enthalpies range between 30–50 kJ mol^{-1}. MTV composition induces an initial drop in activation enthalpy, from 50 kJ mol^{-1} in 0 mol% matrix to 33 kJ mol^{-1} in both 5 and 12 mol% samples, showing a slight steady increase in enthalpy to 44 and 45 kJ mol^{-1} in 27 and 100 mol%, respectively. The HT region ranges between 60–100 kJ mol^{-1} with similar behavior *vs.* PNA content, showing a decrease from 80 kJ mol^{-1} (0% mol MOF) to 60 kJ mol^{-1} (5 mol% MOF), with also an increase to 80 kJ mol^{-1} (27 mol%) and 98 kJ mol^{-1}

100 mol%). Further evidence on the activated nature of the relaxation and the entropy effects by multivariate composition can be observed in the Fig. 4f, which displays a linear relation between activation enthalpies and entropies for all compositions in both temperature regimes. This observation is consistent with the Meyer–Neldel compensation rule,[38] which states that in thermally activated processes between samples of similar composition, changes in activation energy are proportional to the possible number of pathways to achieve the activated state. This trend has been observed in other small molecules and polymer blends,[39,40] and evidences the thermodynamic effects of the MOF solid-solutions.

The average unit cell of the PIZOF-2 MOF (CCDC code OXOLET)[3] in $Fd\bar{3}m$ symmetry, shows positional and dynamic disorder around the phenylene rings in the MOF. Furthermore, we have observed variable rates of phenylene ring rotation depending on their location in the unit cell.[41] A crystal model of 100 mol% PNA PIZOF in $R3$ space group symmetry (Fig. S99†) exhibits steric crowding around the central ring caused by nitro and amino groups, perhaps inhibiting rotational degrees of freedom. A similar situation occurs in the 0 mol% MOF matrix ($F4_132$, Fig. S100†), as the methyl groups also may induce steric crowding reducing molecular motion. Qualitatively, the relative low values of ε' and ε'' suggest little permittivity and little losses, indicating that perhaps PNA does not respond to alternating fields due to: (a) dipolar relaxation modes are outside the frequency range, or (b) PNA moiety is not as dynamic in the crystal, and we only observe rotational dynamics of the benzoate phenylene rings and/or methyl groups. Future studies include assessment dielectric spectroscopy studies in larger single-crystalline samples for dielectric strength and dipole moment elucidation.

Conclusions

In this work, a library of multivariate metal–organic frameworks (MTV MOFs) were prepared from mixtures of soluble nonpolar and polar links that contain *p*-nitroaniline (PNA). The MTV library exhibited the formation of a partial solid solution up to 30 mol%, with linear relation between input and output PNA concentration and a slope less than 1, indicating low tolerance for miscibility of the links. The library exhibits the photophysics of dipole–dipole hypsochromic coupling (H-coupling) by the appearance of a blue-shifted band in the Kubelka–Munk function of the MTV library in PNA concentrations above 5 mol%. We also observed dielectric relaxation that exhibits changes in activation enthalpies at 200 K in the broadband dielectric spectra, as well as dielectric compensation of the Meyer–Neldel type by the linear relation between activation enthalpies and entropies. We demonstrated that MTV MOFs enable systematic study of molecular traits imposed in crystals with constant crystal structure and variable composition.

Data availability

The data supporting article "A multivariate library of zirconia metal–organic frameworks with dissolved *p*-nitroaniline dipoles and concentration dependent optivcal and dielectric response" by Langlois *et al.*, have been included as part of the ESI;† also, a crystallographic information file (CIF) has been submitted to the Cambridge Structural Database, deposition number CCDC 2455083.

Author contributions

Langlois synthesized MOFs, prepared samples, performed measurements, analysed data, wrote manuscript. Wang, Fnu, Harper and Zhai performed measurements, analysed data. Newsome synthesized links. Uribe-Romo conceived the project, directed research analysed data, wrote manuscript.

Conflicts of interest

There are no conflicts to declare.

Acknowledgements

This work was supported by the National Science Foundation Office of Advanced Cyberstructure (Award# 2118201). Dielectric spectroscopy measurements were performed at the Oak Ridge National Laboratory's Center for Nanophase Materials Sciences, which is a DOE Office of Science User Facility.

Notes and references

1 O. M. Yaghi, Complexity and Heterogeneity in MOFs, *In Introduction to Reticular Chemistry*, 2019, pp. 121–144.
2 H. Deng, C. J. Doonan, H. Furukawa, R. B. Ferreira, J. Towne, C. B. Knobler, B. Wang and O. M. Yaghi, Multiple Functional Groups of Varying Ratios in Metal-Organic Frameworks, *Science*, 2010, **327**, 846–850.
3 A. Schaate, P. Roy, T. Preuße, S. J. Lohmeier, A. Godt and P. Behrens, Porous Interpenetrated Zirconium–Organic Frameworks (PIZOFs): A Chemically Versatile Family of Metal–Organic Frameworks, *Chem. – Eur. J.*, 2011, **17**, 9320–9325.
4 J. Lippke, B. Brosent, T. von Zons, E. Virmani, S. Lilienthal, T. Preuße, M. Hülsmann, A. Schneider, S. Wuttke, P. Behrens and A. Godt, Expanding the Group of Porous Interpenetrated Zr-Organic Frameworks (PIZOFs) with Linkers of Different Lengths, *Inorg. Chem.*, 2017, **56**, 748–761.
5 A. H. Assen, K. Adil, K. E. Cordova and Y. Belmabkhout, The chemistry of metal–organic frameworks with face-centered cubic topology, *Coord. Chem. Rev.*, 2022, **468**, 214644.
6 W. J. Newsome, S. Ayad, J. Cordova, E. W. Reinheimer, A. D. Campiglia, J. K. Harper, K. Hanson and F. J. Uribe-Romo, Solid State Multicolor Emission in Substitutional Solid Solutions of Metal–Organic Frameworks, *J. Am. Chem. Soc.*, 2019, **141**, 11298–11303.

7 R. J. Marshall, Y. Kalinovskyy, S. L. Griffin, C. Wilson, B. A. Blight and R. S. Forgan, Functional Versatility of a Series of Zr Metal–Organic Frameworks Probed by Solid-State Photoluminescence Spectroscopy, *J. Am. Chem. Soc.*, 2017, **139**, 6253–6260.
8 X. Chen, B. B. Mendes, Y. Zhuang, J. Conniot, S. Mercado Argandona, F. Melle, D. P. Sousa, D. Perl, A. Chivu, H. K. Patra, W. Shepard, J. Conde and D. Fairen-Jimenez, *J. Am. Chem. Soc.*, 2024, **146**, 1644–1656.
9 G. S. Mohammad-Pour, K. O. Hatfield, D. C. Fairchild, K. Hernandez-Burgos, J. Rodríguez-López and F. J. Uribe-Romo, A Solid-Solution Approach for Redox Active Metal–Organic Frameworks with Tunable Redox Conductivity, *J. Am. Chem. Soc.*, 2019, **141**(51), 19978–19982.
10 W. J. Newsome, A. Chakraborty, R. T. Ly, G. S. Pour, D. C. Fairchild, A. J. Morris and F. J. Uribe-Romo, J-dimer emission in interwoven metal–organic frameworks, *Chem. Sci.*, 2020, **11**(17), 4391–4396.
11 M. Sk, S. Barman, S. Paul, R. De, S. Sreekumar, H. Reinsch, M. Grzywa, N. Stock, D. Volkmer, S. Biswas and S. Roy, An Anthracene-Based Metal-Organic Framework for Selective Photo-Reduction of Carbon Dioxide to Formic Acid Coupled with Water Oxidation, *Chem. – Eur. J.*, 2021, **27**, 4098–4107.
12 H. Furukawa, F. Gándara, Y.-B. Zhang, J. Jiang, W. L. Queen, M. R. Hudson and O. M. Yaghi, Water Adsorption in Porous Metal–Organic Frameworks and Related Materials, *J. Am. Chem. Soc.*, 2024, **136**, 4369–4381.
13 J. I. Furst, J. T. Bryant, K. R. Langlois, S. D. Myers, A. Rahmani, D. C. Fairchild, R. Mehta, T. Jurca, J. B. Benedict and F. J. Uribe-Romo, Vegard's law in multivariate libraries of porous interpenetrated zirconia organic frameworks, *Inorg. Chem. Front.*, 2024, **11**(10), 3021–3027.
14 J. Donohue and K. Trueblood, The crystal structure of p-nitroaniline, *Acta Crystallogr.*, 1956, **9**, 960–965.
15 T. P. Carsey, G. L. Findley and S. P. McGlynn, Systematics in the electronic spectra of polar molecules. 1. Para-disubstituted benzenes, *J. Am. Chem. Soc.*, 1979, **101**(16), 4502–4510.
16 K. Chitoku and K. Higasi, Dielectric Relaxation and Molecular Structure. III. Relaxation Times of Aniline Derivatives in Benzene and Dioxane, *Bull. Chem. Soc. Jpn.*, 1966, **39**, 2160–2168.
17 S. Shigeto, H. Hiramatsu and H.-o. Hamaguchi, Structure and Dipole Moments of the Two Distinct Solvated Forms of p-Nitroaniline in Acetonitrile/CCl4 As Studied by Infrared Electroabsorption Spectroscopy, *J. Phys. Chem. A*, 2006, **110**(10), 3738–3743.
18 D. Kosenkov and L. V. Slipchenko, Solvent Effects on the Electronic Transitions of p-Nitroaniline: A QM/EFP Study, *J. Phys. Chem. A*, 2011, **115**(4), 392–401.
19 T. W. Panunto, Z. Urbanczyk-Lipkowska, R. Johnson and M. C. Etter, Hydrogen-bond formation in nitroanilines: the first step in designing acentric materials, *J. Am. Chem. Soc.*, 1987, **109**(25), 7786–7797.
20 M. S. Dionisio, J. J. Moura-Ramos and G. Williams, Molecular motions in poly(vinyl acetate) and in poly(vinyl acetate)/p-nitroaniline mixtures, *Polymer*, 1993, **34**, 4105–4110.
21 S. Millefiori, G. Favini, A. Millefiori and D. Grasso, Electronic spectra and structure of nitroanilines, *Spectrochim. Acta, Part A*, 1977, **33**(1), 21–27.
22 Z. Dominguez, T.-A. V. Khuong, H. Dang, C. N. Sanrame, J. E. Nuñez and M. A. Garcia-Garibay, Molecular Compasses and Gyroscopes with Polar Rotors: Synthesis and Characterization of Crystalline Forms, *J. Am. Chem. Soc.*, 2003, **125**(29), 8827–8837.
23 N. Aguilar-Valdez, M. Maldonado-Domínguez, R. Arcos-Ramos, M. Romero-Ávila, R. Santillan and N. Farfán, Synthesis of steroidal molecular compasses: exploration of the controlled assembly of solid organic materials, *CrystEngComm*, 2017, **19**(13), 1771–1777.
24 M. A. van der Veen, J. Van Noyen, B. F. Sels, P. A. Jacobs, T. Verbiest and D. E. De Vos, Mapping of the organization of p-nitroaniline in SAPO-5 by second-harmonic generation microscopy, *Phys. Chem. Chem. Phys.*, 2010, **12**, 10688–10692.
25 K. Fabrizio, Khoa N. Le, A. B. Andreeva, C. H. Hendon and C. K. Brozek, Determining Optical Band Gaps of MOFs. ACS, *Mater. Lett.*, 2022, **4**, 457–463.
26 C. Majumder, H. Mizuseki and Y. Kawazoe, Effect of substituent groups on the electronic properties of a molecular device: an ab initio theoretical study, *J. Mol. Struct.: THEOCHEM*, 2004, **681**, 65–69.
27 N. J. Hestand and F. C. Spano, Expanded Theory of H- and J-Molecular Aggregates: The Effects of Vibronic Coupling and Intermolecular Charge Transfer, *Chem. Rev.*, 2018, **118**(15), 7069–7163.
28 C. M. Pochas, K. A. Kistler, H. Yamagata, S. Matsika and F. C. Spano, Contrasting Photophysical Properties of Star-Shaped vs Linear Perylene Diimide Complexes, *J. Am. Chem. Soc.*, 2013, **135**, 3056–3066.
29 H. Yoo, S. Furumaki, J. Yang, J.-E. Lee, H. Chung, T. Oba, H. Kobayashi, B. Rybtchinski, T. M. Wilson, M. R. Wasielewski, M. Vacha and D. Kim, Excitonic Coupling in Linear and Trefoil Trimer Perylenediimide Molecules Probed by Single-Molecule Spectroscopy, *J. Phys. Chem. B*, 2012, **116**, 12878–12886.
30 J. Gierschner and S. Y. Park, Luminescent distyrylbenzenes: tailoring molecular structure and crystalline morphology, *J. Mater. Chem. C*, 2013, **1**, 5818–5832.
31 M. Treger, A. Hannebauer, A. Schaate, J. L. Budde, P. Behrens and A. M. Schneider, Tuning the optical properties of the metal–organic framework UiO-66 via ligand functionalization, *Phys. Chem. Chem. Phys.*, 2023, **25**(8), 6333–6341.
32 W. H. H. Woodward, Broadband Dielectric Spectroscopy—A Practical Guide, *ACS Symp. Ser.*, 2021, 3–59.
33 S. Devautour-Vinot, G. Maurin, C. Serre, P. Horcajada, D. Paula da Cunha, V. Guillerm, E. de Souza Costa, F. Taulelle and C. Martineau, Structure and Dynamics of the Functionalized MOF Type UiO-66(Zr): NMR and Dielectric Relaxation Spectroscopies Coupled with DFT Calculations, *Chem. Mater.*, 2012, **24**(11), 2168–2177.

34 S. Devautour-Vinot, G. Maurin, C. Serre, P. Horcajada, D. Paula da Cunha, V. Guillerm, E. de Souza Costa, F. Taulelle and C. Martineau, Structure and Dynamics of the Functionalized MOF Type UiO-66(Zr): NMR and Dielectric Relaxation Spectroscopies Coupled with DFT Calculations, *Chem. Mater.*, 2012, **24**, 2168–2177.

35 S. Frunza, A. Schönhals, L. Frunza, P. Ganea, H. Kosslick, J. Harloff and A. Schulz, Molecular Relaxation Processes in a MOF-5 Structure Revealed by Broadband Dielectric Spectroscopy: Signature of Phenylene Ring Fluctuations, *J. Phys. Chem. B*, 2010, **114**(40), 12840–12846.

36 S. Balčiūnas, D. Pavlovaitė, M. Kinka, J.-Y. Yeh, P.-C. Han, F.-K. Shieh, K. C.-W. Wu, M. Šimėnas, R. Grigalaitis and J. Banys, Dielectric Spectroscopy of Water Dynamics in Functionalized UiO-66 Metal-Organic Frameworks, *Molecules*, 2020, **25**(8), 1962.

37 Z. Liu, Y. Wang and M. A. Garcia-Garibay, Rotational Dynamics of an Amphidynamic Zirconium Metal–Organic Framework Determined by Dielectric Spectroscopy, *J. Phys. Chem. Lett.*, 2021, **12**(24), 5644–5648.

38 A. Yelo and B. Movagar, Microscoipic explanation of the Compensation (Meyer-Nelder) Rule, *Phys. Rev. Lett.*, 1990, **65**, 618–620.

39 S. Hossain, *MS Thesis*, Lakehead University, 1982.

40 S. Napolitano, Enthalpy-entropy compensation in the slow Arrhenius process, *J. Chem. Phys.*, 2023, **159**, 161103.

41 A. Torres-Huerta, D. Galicia-Badillo, A. Aguilar-Granda, J. T. Bryant, F. J. Uribe-Romo and B. Rodríguez-Molina, Multiple rotational rates in a guest-loaded, amphidynamic zirconia metal–organic framework, *Chem. Sci.*, 2020, **11**(42), 11579–11583.